

Optical pulse-induced quantum geometric waves in graphene

Luis F. Cárdenas-Castillo¹ and Wei Chen²

^{1,2}*Department of Physics, PUC-Rio, 22451-900 Rio de Janeiro, Brazil*

¹lcardenasc@aluno.puc-rio.br

(June 12, 2026)

Abstract

We show that, under a short optical pulse, the quantum metric of Bloch states in the momentum-time (k_x, k_y, t) of graphene becomes dynamic and exhibits a wave-like behavior near Dirac points. This quantum metric wave reflects the Floquet-band structure caused by the pulse, as revealed by solving the time-dependent Schrödinger equation assuming that correlations and out-of-equilibrium effects can be ignored. The momentum and temporal components of the metric have very distinct time dependence that persists even after the pulse has passed. In addition, the pulse also generates a Berry curvature wave that is otherwise absent in static graphene. The time-dependent electron densities in conduction and valence bands also give rise to a Fisher information wave that constitutes part of the quantum metric wave, and is readily measurable by pump-probe experiments.

Keywords: quantum metric; Berry curvature; graphene; Fisher information.

Contents

1	Introduction	1
2	Driven two-band model for graphene under optical pulse	3
2.1	Driven honeycomb-lattice Hamiltonian	3
2.2	Pulse-induced driven quantum tunneling in graphene	4
3	Quantum geometry and information geometry in momentum-time	4
3.1	Quantum geometric tensor in momentum-time	4
3.2	Quantum geometric waves	5
3.3	Fisher information waves	7
4	Conclusions	9
5	Acknowledgments	10
A	Driven quantum tunneling under rotating wave approximation	10
B	Dynamic quantum geometry in the whole Brillouin zone	12

1 Introduction

The quantum geometry of Bloch states in the momentum space of solids has emerged as an important topic that is currently under intensive investigation. This notion of quantum geometry

arises when one considers the overlap between neighboring Bloch states in a D -dimensional momentum space, whose leading-order expansion defines a quantum geometric tensor. The real part of the tensor gives the quantum metric [1], while the imaginary part gives the Berry curvature that encodes geometric phases and many topological and transport properties [2, 3]. Particularly in semiconductors and insulators, this quantum metric coincides with the optical transition matrix elements of interband transitions [4, 5], and thus a wide variety of dielectric and optical properties, such as optical conductivity, dielectric function, refractive index, absorption coefficient, reflectance, etc, are all determined by the quantum metric [6, 7], which has stimulated a great deal of interest on the quantum metric.

Beyond in static systems, quantum geometry in time-dependent systems has also been an intriguing issue that manifests many unique features that are absent in their static counterparts [8–13]. Firstly, because the time dependence of the quantum state is no longer described by a simple dynamic phase factor, time itself serves as an additional parameter that promotes the geometry to a $(D + 1)$ -dimensional momentum-time quantum geometry. The quantum metric in this case is in a way analogous to the spacetime metric in classical gravity, although one should keep in mind that momentum-time is a Euclidean manifold, unlike the Lorentzian manifold of spacetime. Secondly, the time dependence of the quantum state also renders the quantum metric time-dependent. In most situations, the dynamic quantum metric oscillates in a wavy fashion, of which we call a quantum-metric wave, serving as an analog of the gravitational wave in general relativity, although many components of the quantum metric wave are highly nonlinear and do not behave like a simple sinusoidal wave.

To elaborate these unique features in time-dependent systems, and also motivated by the optical effects related to static quantum metric, we resort to the quantum geometry of graphene in the setup of pump-probe experiments [14–26]. In this type of experiment, a short laser pulse of sub-picosecond duration is applied to graphene, causing nonequilibrium excitations of electrons from the valence to conduction bands, which then relax back to equilibrium via rather complicated many-body interactions. This subject has been investigated intensively owing to the rich out-of-equilibrium physics involved, such as the Floquet band formation, light-induced pseudospin textures, and pump-probe photoemission [27–29]. To capture the essential features of the dynamic quantum geometry by the simplest approach, we solve the time-dependent Schrödinger equation in momentum space under the influence of the pulse [30], while ignoring all the complications coming from out-of-equilibrium and many-body effects. We anticipate that such a simplified approach can capture the evolution of quantum metric during a relatively weak pulse, while it is unable to describe the relaxation back to equilibrium long after the pulse. Using this simple approach, we quantify the momentum and temporal dependence of the quantum metric in the three-dimensional (3D) momentum-time (k_x, k_y, t) , revealing intriguing wave-like patterns that coincide with the Floquet bands. Remarkably, we find that the laser pulse also generates a Berry curvature wave in the momentum-time mainly distributed around the Dirac point, which is absent in an otherwise static graphene, pointing to the significance of optical engineering of quantum geometric properties.

To relate the quantum metric wave to experimental observables, we further invoke the aspects of information geometry into the problem [31]. We elaborate that from the time-varying valence and conduction electron densities, a Fisher information matrix [32] can be introduced to quantify the information that can be extracted from the electron density as a time-varying probability mass function. The Fisher information matrix constitutes part of the dynamic quantum metric [33], and can be extracted from the time-varying valence and conduction electron densities measured by time- and angle-resolved photoemission spectroscopy (tr-ARPES), suggesting that the information geometry part of the dynamic quantum geometry can be readily measured.

2 Driven two-band model for graphene under optical pulse

2.1 Driven honeycomb-lattice Hamiltonian

In this section, we formulate the coherently driven two-band description of graphene and specify the pure-state interband dynamics underlying the quantum geometry. We start from a monolayer graphene described within a nearest-neighbor tight-binding model on the honeycomb lattice [34]. In the sublattice basis (A, B), the static Bloch Hamiltonian is

$$H_0(\mathbf{k}) = \begin{pmatrix} 0 & d_1(\mathbf{k}) - id_2(\mathbf{k}) \\ d_1(\mathbf{k}) + id_2(\mathbf{k}) & 0 \end{pmatrix} \quad (1)$$

with

$$\begin{aligned} d_1(\mathbf{k}) &= \gamma[\cos \mathbf{k} \cdot \mathbf{a}_1 + \cos \mathbf{k} \cdot \mathbf{a}_2 + 1] \\ d_2(\mathbf{k}) &= \gamma[\sin \mathbf{k} \cdot \mathbf{a}_1 + \sin \mathbf{k} \cdot \mathbf{a}_2]. \end{aligned} \quad (2)$$

Here $\gamma = 2.6$ eV is the nearest-neighbor hopping amplitude [35], $\mathbf{a}_1 = a(3/2, \sqrt{3}/2)$ and $\mathbf{a}_2 = a(3/2, -\sqrt{3}/2)$ are the primitive lattice vectors, and $a = 1.42$ Å is the carbon-carbon distance. The conduction and valence band energies are $E_c(\mathbf{k}) = +d(\mathbf{k})$ and $E_v(\mathbf{k}) = -d(\mathbf{k})$, respectively, where $d(\mathbf{k}) = \sqrt{d_1^2(\mathbf{k}) + d_2^2(\mathbf{k})}$.

The optical pump is incorporated through the Peierls substitution by means of a time-dependent vector potential $\mathbf{A}(t) = (A_x(t), A_y(t)) = \hat{\mathbf{e}}V(t)$, where $\hat{\mathbf{e}}$ specifies the polarization direction, and $V(t)$ describes the sinusoidal oscillation and Gaussian envelope of the pulse shape

$$V(t) = \frac{A_0}{\sqrt{2\pi\tau}} \exp\left[-\frac{(t-t_0)^2}{2\tau^2}\right] \sin(\Omega t). \quad (3)$$

The factor A_0 fixes the overall strength of the vector potential, chosen such that the corresponding electric field $\mathbf{E}(t) = -\partial_t \mathbf{A}(t)$ has a total fluence [21]

$$F = \frac{\epsilon_0 c}{2} \int dt |\mathbf{E}(t)|^2 = 4.6 \text{ mJ cm}^{-2}. \quad (4)$$

In Eq. (3), t_0 specifies the pulse center, τ controls the envelope width, and Ω is the carrier frequency. Throughout the paper, we choose $\hbar\omega_{\text{pump}} = \hbar\Omega = 950$ meV, $\tau = 18$ fs, $t_0 = 70$ fs and chemical potential $\mu = 0$, to simulate a typical pump-probe experiment [21].

The drive enters the tight-binding Hamiltonian through the Peierls substitution

$$\theta_i(t) = \frac{e}{\hbar} \int_r^{r+\delta_i} \mathbf{A}(t) \cdot d\mathbf{x} \quad (5)$$

where δ_i are the nearest-neighbor vectors of graphene:

$$\delta_1 = a\left(\frac{1}{2}, \frac{\sqrt{3}}{2}\right), \quad \delta_2 = a\left(\frac{1}{2}, -\frac{\sqrt{3}}{2}\right), \quad \delta_3 = a(-1, 0) \quad (6)$$

Evaluating the line integral along the three bonds, we obtain

$$\begin{aligned} \theta_1(t) &= \alpha_P \left(\frac{1}{2} A_x(t) + \frac{\sqrt{3}}{2} A_y(t) \right) \\ \theta_2(t) &= \alpha_P \left(\frac{1}{2} A_x(t) - \frac{\sqrt{3}}{2} A_y(t) \right) \\ \theta_3(t) &= -\alpha_P A_x(t) \end{aligned} \quad (7)$$

where $\alpha_P = ea/\hbar$, which modifies the \mathbf{d} -vector in Eq. (2) by

$$\begin{aligned}\tilde{d}_1(\mathbf{k}, t) &= \gamma[\cos(\mathbf{k} \cdot \mathbf{a}_1 - \theta_1(t)) + \cos(\mathbf{k} \cdot \mathbf{a}_2 - \theta_2(t)) + \cos(\theta_3(t))], \\ \tilde{d}_2(\mathbf{k}, t) &= \gamma[\sin(\mathbf{k} \cdot \mathbf{a}_1 - \theta_1(t)) + \sin(\mathbf{k} \cdot \mathbf{a}_2 - \theta_2(t)) - \sin(\theta_3(t))].\end{aligned}\quad (8)$$

Since many features revealed by our numerical results in the following sections are found to be robust against the direction of polarization, we will only present the results for the polarization along the armchair direction $\mathbf{A} = (A_x(t), 0)$ for simplicity.

2.2 Pulse-induced driven quantum tunneling in graphene

In terms of the dimensionless $n_1(\mathbf{k}) = d_1(\mathbf{k})/d(\mathbf{k})$ and $n_2(\mathbf{k}) = d_2(\mathbf{k})/d(\mathbf{k})$ that satisfy $n_1^2(\mathbf{k}) + n_2^2(\mathbf{k}) = 1$, the conduction $|u_c(\mathbf{k})\rangle$ and valence $|u_v(\mathbf{k})\rangle$ band eigenstates of the static Hamiltonian $H_0(\mathbf{k})$ in Eq. (1) are

$$|u_c(\mathbf{k})\rangle = \frac{1}{\sqrt{2}} \begin{pmatrix} 1 \\ n_1(\mathbf{k}) + in_2(\mathbf{k}) \end{pmatrix}, \quad |u_v(\mathbf{k})\rangle = \frac{1}{\sqrt{2}} \begin{pmatrix} 1 \\ -n_1(\mathbf{k}) - in_2(\mathbf{k}) \end{pmatrix}. \quad (9)$$

To analyze the driven dynamics, we follow the formalism of driven quantum tunneling to expand the time-dependent state by the static eigenstates [30]

$$|\Psi(\mathbf{k}, t)\rangle = c_1(\mathbf{k}, t)e^{-id(\mathbf{k})t/\hbar}|u_c(\mathbf{k})\rangle + c_2(\mathbf{k}, t)e^{+id(\mathbf{k})t/\hbar}|u_v(\mathbf{k})\rangle, \quad (10)$$

which evolves according to the time-dependent Schrödinger equation

$$i\hbar\partial_t|\Psi(\mathbf{k}, t)\rangle = H(\mathbf{k}, t)|\Psi(\mathbf{k}, t)\rangle. \quad (11)$$

In terms of the two real functions that encode the pulse and momentum dependence

$$\begin{aligned}\Xi(\mathbf{k}, t) &= \frac{1}{\hbar}[d(\mathbf{k}) - \tilde{d}_1(\mathbf{k}, t)n_1(\mathbf{k}) - \tilde{d}_2(\mathbf{k}, t)n_2(\mathbf{k})] \\ \Lambda(\mathbf{k}, t) &= \frac{1}{\hbar}[\tilde{d}_1(\mathbf{k}, t)n_2(\mathbf{k}) - \tilde{d}_2(\mathbf{k}, t)n_1(\mathbf{k})]\end{aligned}\quad (12)$$

the Schrödinger equation leads to the equations of motion for the amplitudes

$$\begin{aligned}\dot{c}_1(\mathbf{k}, t) &= i\Xi(\mathbf{k}, t)c_1(\mathbf{k}, t) - \Lambda(\mathbf{k}, t)e^{+2id(\mathbf{k})t/\hbar}c_2(\mathbf{k}, t), \\ \dot{c}_2(\mathbf{k}, t) &= -i\Xi(\mathbf{k}, t)c_2(\mathbf{k}, t) + \Lambda(\mathbf{k}, t)e^{-2id(\mathbf{k})t/\hbar}c_1(\mathbf{k}, t),\end{aligned}\quad (13)$$

indicating that the function $\Xi(\mathbf{k}, t)$ describes a drive-induced intraband phase modulation, whereas $\Lambda(\mathbf{k}, t)$ controls the interband coupling. To draw relevance to pump-probe experiments, we assume that before the pulse kicks in at $t = 0$, all the electrons are in the valence band states $|\Psi(\mathbf{k}, t = 0)\rangle = |u_v(\mathbf{k})\rangle$, leading to the initial condition for the complex amplitudes

$$(\text{Re } c_1(\mathbf{k}, 0), \text{Im } c_1(\mathbf{k}, 0), \text{Re } c_2(\mathbf{k}, 0), \text{Im } c_2(\mathbf{k}, 0)) = (0, 0, 1, 0). \quad (14)$$

Equation (13) can then be solved numerically at each momentum \mathbf{k} on an $N_k \times N_k$ grid, where we used $N_k = 31$.

3 Quantum geometry and information geometry in momentum-time

3.1 Quantum geometric tensor in momentum-time

Our goal is to examine the quantum geometry of the time-dependent state $|\Psi(\mathbf{k}, t)\rangle$ in the momentum-time $\boldsymbol{\lambda} = (k_x, k_y, t)$ treated as a 3D Euclidean manifold. Since the state is properly

normalized $|c_1(\mathbf{k}, t)|^2 + |c_2(\mathbf{k}, t)|^2 = 1$ at any point in momentum-time, one can introduce the quantum geometric tensor of this state by

$$Q_{\mu\nu}(\lambda) = \langle \partial_\mu \Psi(\lambda) | \partial_\nu \Psi(\lambda) \rangle - \langle \partial_\mu \Psi(\lambda) | \Psi(\lambda) \rangle \langle \Psi(\lambda) | \partial_\nu \Psi(\lambda) \rangle, \quad (15)$$

where $\partial_\mu = \partial/\partial\lambda^\mu$ is the derivative on either the momentum or time calculated numerically by means of the finite difference on the grid. The real part of the tensor defines the time-dependent quantum metric

$$g_{\mu\nu}(\lambda) = \text{Re } Q_{\mu\nu}(\lambda), \quad (16)$$

which characterizes the overlap of the time-dependent states on neighboring points on the momentum-time manifold (repeating indices are summed)

$$|\langle \Psi(\mathbf{k}, t) | \Psi(\mathbf{k} + \delta\mathbf{k}, t + \delta t) \rangle|^2 = 1 - g_{\mu\nu}(\mathbf{k}, t) \delta\lambda^\mu \delta\lambda^\nu. \quad (17)$$

On the other hand, the imaginary part of the tensor gives a time-dependent Berry curvature,

$$\Omega_{\mu\nu}(\lambda) = -2 \text{Im } Q_{\mu\nu}(\lambda), \quad (18)$$

that is known to be absent in static graphene.

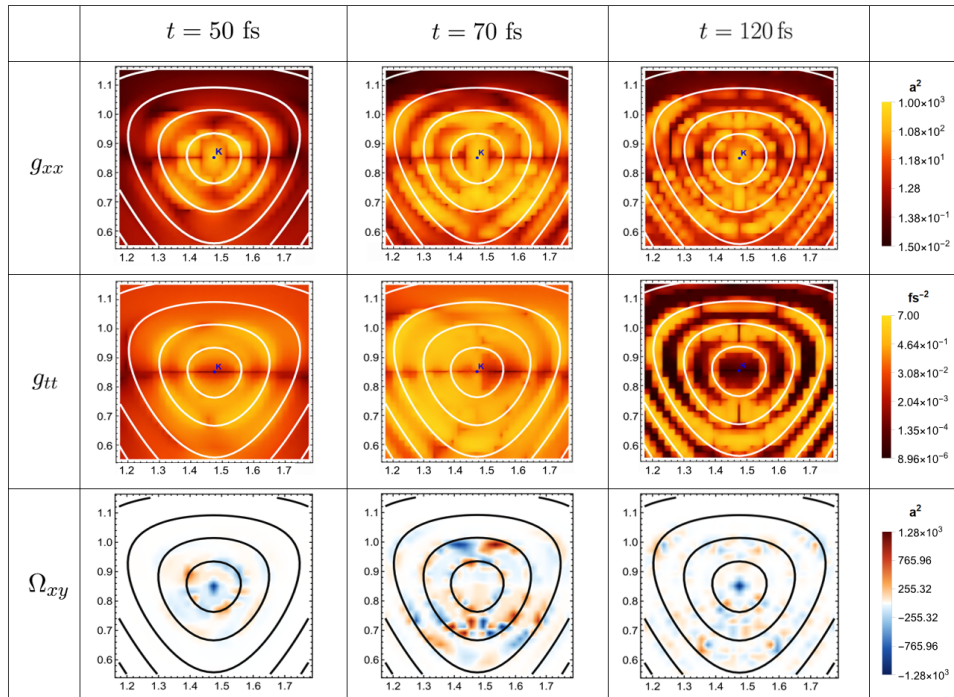


Figure 1: Momentum profile of the elements of the dynamic quantum geometric tensor near the K valley under the influence of an x -polarized optical pulse at the beginning of the pulse $t = 50$ fs, at the peak of the pulse $t = 70$ fs, and after the pulse $t = 120$ fs. The panels show the momentum-space quantum metric g_{xx}/a^2 , the temporal metric g_{tt}/fs^{-2} , and the Berry curvature Ω_{xy}/a^2 , all of which manifest ring-like features that respect the Floquet bands labeled by white and black contours.

3.2 Quantum geometric waves

Figure 1 shows numerical results near the K -valley, where we present the momentum g_{xx} and temporal g_{tt} components of the quantum metric, as well as the momentum component of the

Berry curvature Ω_{xy} . We present the results at the beginning of the pulse $t = 50$ fs, close to the peak of the pulse $t = 70$ fs, and right after the pulse $t = 120$ fs. The momentum components $g_{k_\mu k_\nu}$ and $\Omega_{k_\mu k_\nu}$ are plotted in units of a^2 , while the temporal component g_{tt} is plotted in units of fs^{-2} , and the data are presented in logarithmic scale in order to highlight the pattern in momentum space.

All the geometric quantities in Fig. 1 clearly display ring-like features near the K -valley, which we refer to as quantum geometric waves. A similar pattern also appears near the K' -valley, but we omit for simplicity. To further understand the origin of these rings, we plot the contour in momentum space where the optical excitation energy, i.e., energy difference between conduction and valence bands, matches multiples of the photon energy

$$E_c(\mathbf{k}) - E_v(\mathbf{k}) = 2d(\mathbf{k}) = \text{integer} \times \hbar\omega_{\text{pump}}, \quad (19)$$

presented as the white contours in Fig. 1. The coincidence of these resonance contours and the ring-like features of $\{g_{xx}, g_{tt}, \Omega_{xy}\}$ is evident, indicating that the rings are a finite-pulse analogue of Floquet sideband formation [27]. In other words, the quantum geometry of time-dependent systems senses the formation of Floquet bands. Note that while the quantum metric g_{xx} and g_{tt} maintain roughly the same sign along the contour, the Berry curvature Ω_{xy} changes sign along the contour and has a much more complicated pattern around the K -valley. The momentum integration of the Berry curvature remains zero at all times, indicating no Chern number is induced by the pulse.

To further understand the temporal dependence of the quantum geometric waves, we fix the momentum and investigate the evolution of these geometric quantities as a function of time. Specifically, we focus on the high symmetry line connecting the Γ and K points, and around the momentum that satisfies the first resonance condition $E_c(\mathbf{k}) - E_v(\mathbf{k}) = \hbar\omega_{\text{pump}}$ according to Eq. (19). In Fig. 2, we present the results of time dependence at momenta slightly larger than the first resonance and farther away from the K -point $|\mathbf{k}(q)| = 1.5754\text{\AA}^{-1}$, exactly at the resonance $|\mathbf{k}(q)| = 1.6196\text{\AA}^{-1}$, and slightly less than the resonance and closer to the K -point $|\mathbf{k}(q)| = 1.7005\text{\AA}^{-1}$. Each element of the quantum geometric tensor is found to exhibit a very distinct time dependence: The momentum components of the quantum metric $\{g_{xx}, g_{xy}, g_{yy}\}$ oscillate with time even after the pulse has passed, and increase with time in a nonlinear fashion; The temporal component g_{tt} faithfully follows the time dependence of the pulse to display the same oscillation and envelope shape; The mixed component g_{tx} and g_{ty} also follow the pulse shape, but only at the resonant momentum do they increase significantly with time in a linear fashion after the pulse; The momentum component of the Berry curvature Ω_{xy} also oscillates and increases linearly with time; Finally, the mixed component Berry curvature Ω_{xt} and Ω_{yt} follow the pulse shape, and remain roughly constant after the pulse.

To understand the peculiar behavior of each component of the metric, in Appendix A we investigate a toy model of a chain of topological insulator in the presence of an oscillating mass term. The advantage of this toy model is that the time-dependent state $|\Psi(k, t)\rangle$ can be solved analytically under an approximation [30], and so do the quantum metric $g_{\mu\nu}$ and Berry curvature $\Omega_{\mu\nu}$. We find that the time dependence of all the components shown in Fig. 2 can be qualitatively captured by the toy model, indicating that the behavior shown in Fig. 2 is fairly universal for time-dependent systems irrespective of the dimension and the drive. Finally, for completeness, in Appendix B we show the dynamic quantum metric and Berry curvature in a wider range of momentum-time covering the whole Brillouin zone. The result shows that despite some weak responses throughout the Brillouin zone, the induced quantum metric and Berry curvature are the largest near the K and K' valleys.

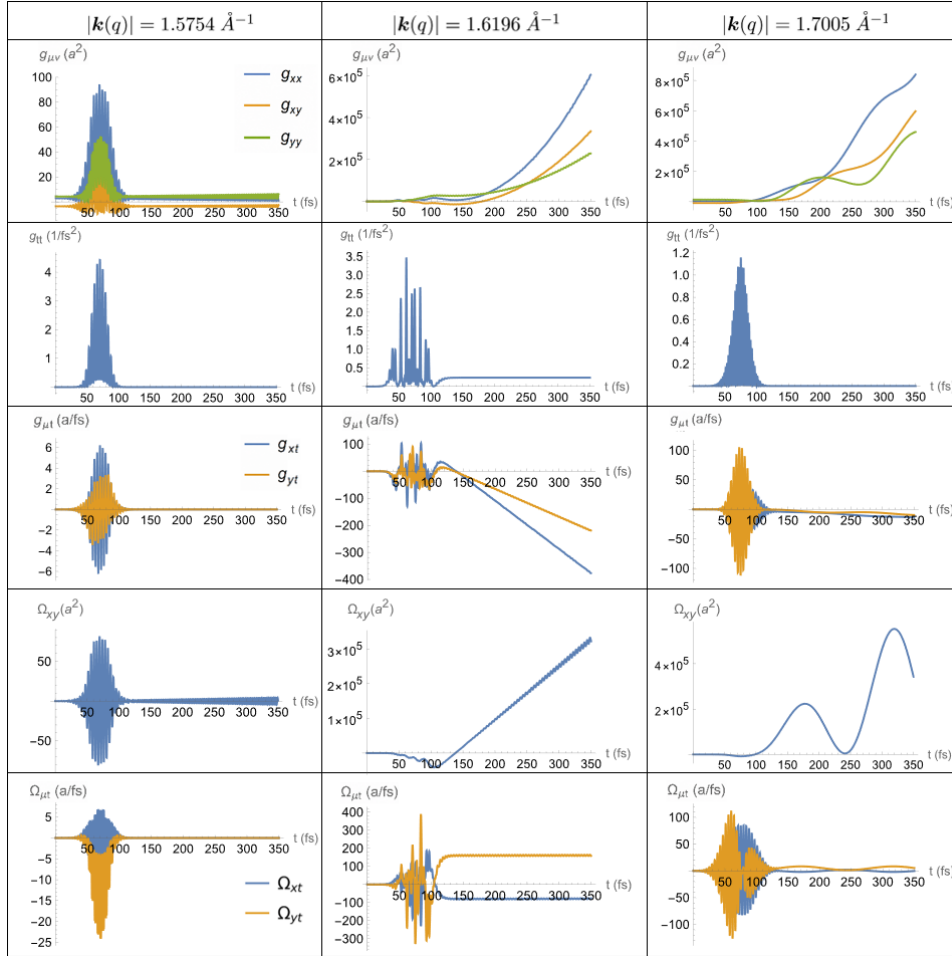


Figure 2: Time dependence of the dynamic quantum geometric tensor along the $\Gamma - K$ direction caused by an x -polarized pulse, evaluated at below $|\mathbf{k}(q)| = 1.5754\text{\AA}^{-1}$, exactly at $|\mathbf{k}(q)| = 1.6196\text{\AA}^{-1}$, and above $|\mathbf{k}(q)| = 1.7005\text{\AA}^{-1}$ the first resonant condition $E_c(\mathbf{k}) - E_v(\mathbf{k}) = \hbar\omega_{\text{pump}}$. We present the momentum component of the quantum metric $\{g_{xx}, g_{xy}, g_{yy}\}$ (first row), temporal component of the metric g_{tt} (second row), mixed component of the metric $\{g_{xt}, g_{yt}\}$ (third row), momentum component of the Berry curvature Ω_{xy} (fourth row), and mixed component of the curvature $\{\Omega_{xt}, \Omega_{yt}\}$ (fifth row).

3.3 Fisher information waves

The quantum metric of the static graphene has been proposed to be measurable by optical means [36], and so does the Berry curvature in other static solids [37–39]. However, for the dynamic quantum metric and Berry curvature predicted in Sec. 3.2 that oscillates in the femtosecond scale, it is currently unclear to us how they can be detected experimentally. Nevertheless, in this section, we elaborate that the Fisher information contribution to the quantum metric can be readily detected by pump-probe experiments. The notion of Fisher information matrix arises when we treat the amplitudes in Eq. (10) as a probability mass function $\{|c_1|^2, |c_2|^2\} = \{P_1, P_2\}$ of finding the state in the two corresponding eigenstates. The Fisher information matrix that describes the variation of the probability mass function in the momentum-time manifold is defined as

$$I_{\mu\nu}(\mathbf{k}, t) = \sum_{i=1}^2 P_i(\mathbf{k}, t) \partial_\mu \ln P_i(\mathbf{k}, t) \partial_\nu \ln P_i(\mathbf{k}, t) = 4 \sum_{i=1}^2 \partial_\mu |c_i(\mathbf{k}, t)| \partial_\nu |c_i(\mathbf{k}, t)| \quad (20)$$

The dynamical quantum metric $g_{\mu\nu}$ is equivalent to a quarter of the Fisher information matrix $I_{\mu\nu}/4$ plus the corrections due to the phase of $c_i(\mathbf{k}, t)$ and the momentum dependence of the basis states [33]. Thus should the amplitudes $\{|c_1|^2, |c_2|^2\}$ be measured experimentally, which can be quantified from the time-dependent spectral weight measured by tr-ARPES [21], the Fisher information matrix can be readily extracted through taking derivatives with respect to momentum and time according to Eq. (20).

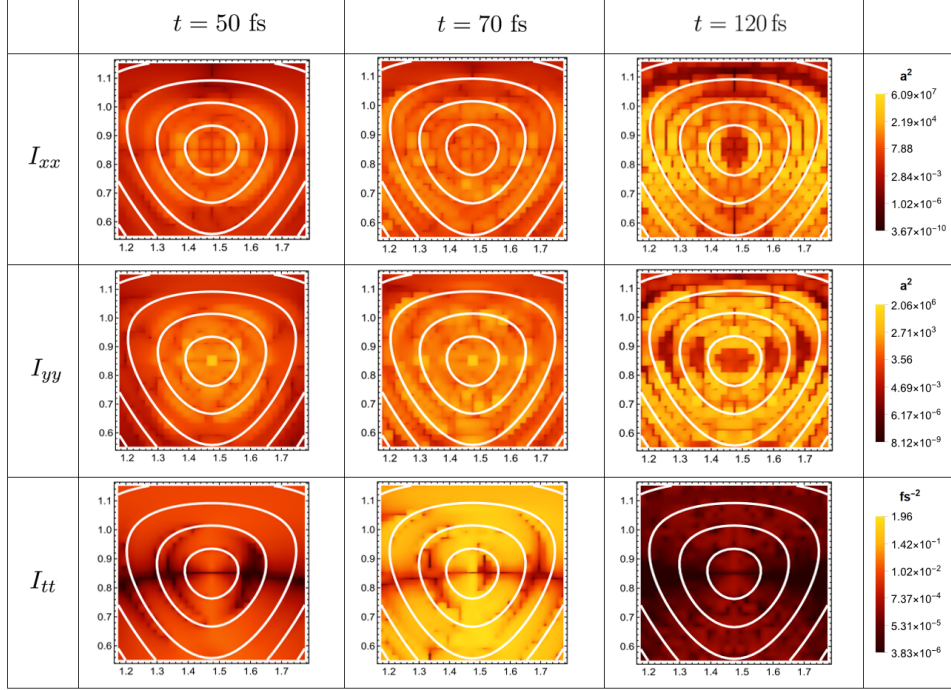


Figure 3: Momentum profile of the dynamic Fisher information matrix near the K valley caused by x -polarized pulse evaluated at time $t = 50, 70, 120$ fs. We present the momentum components I_{xx} and I_{yy} in units of a^2 , and the temporal component I_{tt} in units of fs^{-2} . The white contours label the location of Floquet bands.

Numerical results for the elements of Fisher information matrix $\{I_{xx}, I_{yy}, I_{tt}\}$ near the K -point are shown in logarithmic scale in Fig. 3. The ring-like features that coincide with the Floquet bands are evident, of which we call Fisher information waves, suggesting that the Fisher information constructed from the amplitudes $\{|c_1|^2, |c_2|^2\}$ also senses the formation of Floquet bands [27]. The time dependence of the amplitudes and Fisher information matrix are shown in Fig. 4 for the same three momenta along the $\Gamma - K$ line as Fig. 2, manifesting the following features: The amplitudes $\{|c_1|^2, |c_2|^2\}$ that characterize the population of the two bands oscillate rapidly during the pulse, signifying a fast transition between the two bands caused by the pulse; The momentum components $\{I_{xx}, I_{yy}, I_{xy}\}$ oscillate and increase during the pulse, until reaching a stable configuration after the pulse has passed; The temporal component I_{tt} faithfully follows the pulse shape; The mixed components $\{I_{xt}, I_{yt}\}$ are nonzero during the pulse, but do not completely follow the pulse shape. In Appendix A, we use the aforementioned toy model to analytically corroborate these peculiar behaviors, which suggest that they may be fairly universal in time-dependent systems regardless of the drive.

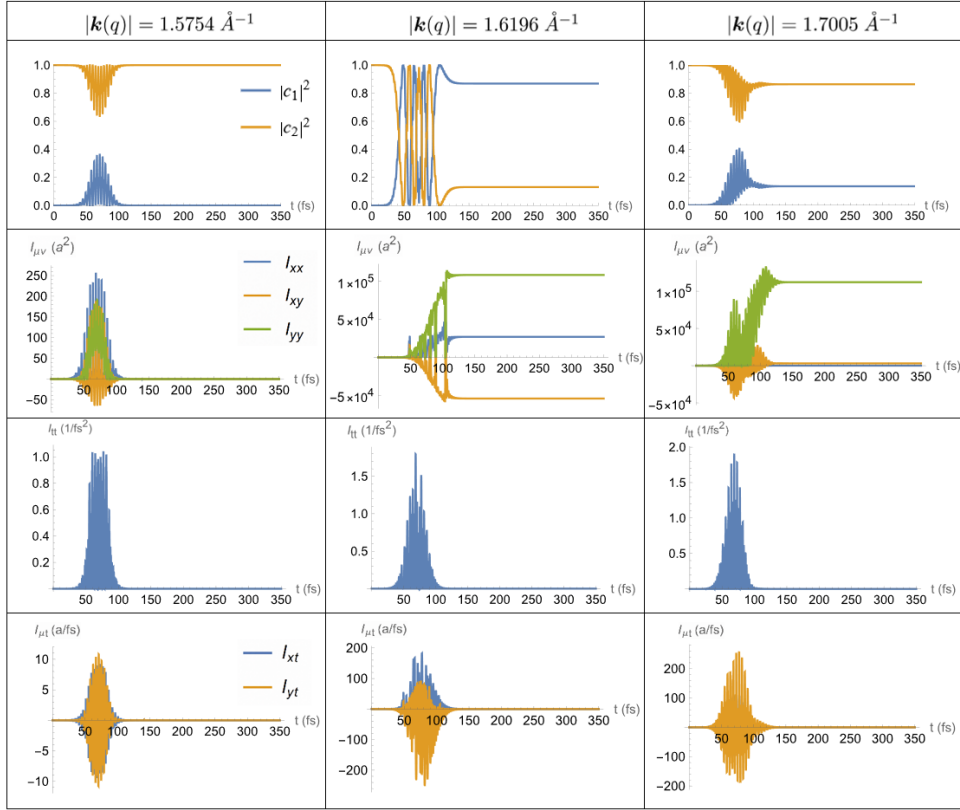


Figure 4: Time-varying band populations $\{|c_1|^2, |c_2|^2\}$ (first row), momentum components $\{I_{xx}, I_{xy}, I_{yy}\}$ (second row), temporal component I_{tt} (third row), and mixed component $\{I_{xt}, I_{yt}\}$ of the dynamic Fisher information matrix along the $\Gamma - K$ direction caused by x -polarized pulse. The columns correspond to momenta below, at, and above the first resonant condition (see caption of Fig. 2).

4 Conclusions

In summary, by means of solving time-dependent Schrödinger equation, we reveal that a short optical pulse causes the quantum metric of graphene in the 3D momentum-time manifold to become dynamic. The resulting quantum metric waves coincide with the Floquet bands caused by the pulse, and each component of the metric is found to have a very distinct time dependence that persists even after the pulse, which can be qualitatively explained by a toy model under the rotating wave approximation. Interestingly, the pulse also generates a Berry curvature wave that is otherwise absent in static graphene. The time dependence of the electron densities in the valence and conduction bands caused by the pulse, which can be viewed as the change of a probability mass function on the momentum-time manifold, further introduces a Fisher information wave that can be readily measured by pump-probe experiments.

We anticipate that the correlations and out-of-equilibrium effects that are not taken into account by our approach can significantly modify these dynamic quantum geometric properties in reality. In fact, when these complications are taken into account and Bloch states are ill-defined, it is even dubious how quantum metric and Berry curvature can be introduced. This profound question certainly deserves to be further investigated under realistic pump-probe experiment setup. Nevertheless, we anticipate that the time-dependent electron densities in the two bands, which have been extracted from the spectral function of tr-ARPES [21], would allow the Fisher information waves to be analyzed without ambiguity. Further comparison with experimental data is required to analyze whether our simple approach provides a reasonable description to

the Fisher information waves in reality.

5 Acknowledgments

We acknowledge the support of the INCT project Advanced Quantum Materials, involving the Brazilian agencies CNPq (Proc. 408766/2024-7), FAPESP, and CAPES. W.C. acknowledges the financial support of the productivity in research fellowship from CNPq.

A Driven quantum tunneling under rotating wave approximation

Our aim in this section is to understand the time dependence of quantum metric, Berry curvature, and Fisher information matrix in Sec. 3.2 and 3.3 by means of a 1D toy model, whose quantum geometric properties can be solved analytically under rotating-wave approximation [30]. For this purpose, we consider the linearized Dirac Hamiltonian in 1D with an oscillating mass term ($\hbar = 1$ throughout this section)

$$H(t) = M \sin \Omega t \sigma_x + k \sigma_y. \quad (21)$$

Physically, this toy model starts as a topological semimetal phase $M = 0$ at $t = 0$, and the mass term M oscillates between positive and negative values at $t > 0$ with frequency Ω . Although the periodically oscillating mass term is fundamentally different from the optical pulse described by Eq. (3), we will see that it gives very similar quantum geometric properties. We expand the time-dependent state of interest by the eigenstates of the time-independent part $k\sigma_y$

$$|\Psi(k, t)\rangle = c_1(t)e^{-ikt} \frac{1}{\sqrt{2}} \begin{pmatrix} 1 \\ i \end{pmatrix} + c_2(t)e^{ikt} \frac{1}{\sqrt{2}} \begin{pmatrix} 1 \\ -i \end{pmatrix}, \quad (22)$$

with the amplitudes satisfying $|c_1(t)|^2 + |c_2(t)|^2 = 1$. The time-dependent Schrödinger equation gives

$$\begin{aligned} & i \frac{d}{dt} \begin{pmatrix} c_1(t)e^{-ikt} + c_2(t)e^{ikt} \\ ic_1(t)e^{-ikt} - ic_2(t)e^{ikt} \end{pmatrix} \\ &= \begin{pmatrix} M \sin \Omega t - ik \\ M \sin \Omega t + ik \end{pmatrix} \begin{pmatrix} c_1(t)e^{-ikt} + c_2(t)e^{ikt} \\ ic_1(t)e^{-ikt} - ic_2(t)e^{ikt} \end{pmatrix}, \end{aligned} \quad (23)$$

leading to the differential equations for the coefficients

$$\begin{aligned} \frac{dc_1}{dt} &= i \frac{M}{2} c_2 \left\{ e^{i(2k+\Omega)t} - e^{i(2k-\Omega)t} \right\}, \\ \frac{dc_2}{dt} &= i \frac{M}{2} c_1 \left\{ e^{-i(2k+\Omega)t} - e^{-i(2k-\Omega)t} \right\}. \end{aligned} \quad (24)$$

In general, these equations have to be solved numerically. Nevertheless, within the rotating wave approximation that drops the $e^{\pm i(2k+\Omega)t}$ terms based on the argument that these oscillations are too fast to induce a substantial transition between the two eigenstates, we can obtain some analytical results. Denoting $\delta = \Omega - 2k$, the approximation amounts to

$$\frac{dc_1}{dt} = -i \frac{M}{2} c_2 e^{-i\delta t}, \quad \frac{dc_2}{dt} = -i \frac{M}{2} c_1 e^{i\delta t}. \quad (25)$$

We adopt the initial condition $c_1(0) = 0$ and $c_2(0) = 1$ such that all the particles are in the valence band at $t = 0$. The solutions are

$$\begin{aligned} c_1 &= -ie^{-i\delta t/2} \frac{M}{\Omega_R} \sin(\Omega_R t/2). \\ c_2 &= e^{i\delta t/2} \left[\cos(\Omega_R t/2) - \frac{i\delta}{\Omega_R} \sin(\Omega_R t/2) \right], \end{aligned} \quad (26)$$

where $\Omega_R = \sqrt{M^2 + \delta^2}$ is the Rabi frequency.

The momentum-time quantum metric in this 2D manifold $k^\mu = (k, t)$ is defined from Eq. (17). To calculate the quantum metric and Berry curvature, we write the state in Eq. (22) as $|\Psi\rangle = c_1(t)e^{-ikt}|u_c\rangle + c_2(t)e^{ikt}|u_v\rangle$. Both $|u_c\rangle$ and $|u_v\rangle$ are independent of (k, t) , so $\partial_\mu|\Psi\rangle = \partial_\mu(c_1e^{-ikt})|u_c\rangle + \partial_\mu(c_2e^{ikt})|u_v\rangle$. Together with $\langle u_\alpha|u_\beta\rangle = \delta_{\alpha\beta}$, the quantum metric and Berry curvature can be calculated conveniently by

$$\begin{aligned} g_{\mu\nu} &= \frac{1}{2}\langle\partial_\mu\Psi|\partial_\nu\Psi\rangle + \frac{1}{2}\langle\partial_\nu\Psi|\partial_\mu\Psi\rangle - \langle\partial_\mu\Psi|\Psi\rangle\langle\Psi|\partial_\nu\Psi\rangle \\ &= \frac{1}{2}\partial_\mu(c_1^*e^{ikt})\partial_\nu(c_1e^{-ikt}) + \frac{1}{2}\partial_\mu(c_2^*e^{-ikt})\partial_\nu(c_2e^{ikt}) \\ &\quad + \frac{1}{2}\partial_\nu(c_1^*e^{ikt})\partial_\mu(c_1e^{-ikt}) + \frac{1}{2}\partial_\nu(c_2^*e^{-ikt})\partial_\mu(c_2e^{ikt}) \\ &\quad - \left[\partial_\mu(c_1^*e^{ikt})(c_1e^{-ikt}) + \partial_\mu(c_2^*e^{-ikt})(c_2e^{ikt}) \right] \left[(c_1^*e^{ikt})\partial_\nu(c_1e^{-ikt}) + (c_2^*e^{-ikt})\partial_\nu(c_2e^{ikt}) \right]. \\ \Omega_{\mu\nu} &= i\langle\partial_\mu\Psi|\partial_\nu\Psi\rangle - i\langle\partial_\nu\Psi|\partial_\mu\Psi\rangle \\ &= i\partial_\mu(c_1^*e^{ikt})\partial_\nu(c_1e^{-ikt}) + i\partial_\mu(c_2^*e^{-ikt})\partial_\nu(c_2e^{ikt}) \\ &\quad - i\partial_\nu(c_1^*e^{ikt})\partial_\mu(c_1e^{-ikt}) - i\partial_\nu(c_2^*e^{-ikt})\partial_\mu(c_2e^{ikt}). \end{aligned} \quad (27)$$

$$(28)$$

By taking straightforward derivatives, these geometric quantities are found to be

$$\begin{aligned} g_{kk} &= \frac{M^2}{2\Omega_R^6} \left(3M^2 + 2\delta^2 \left(2 + t^2\Omega_R^2 \right) - 4\Omega_R^2 \cos(\Omega_R t) + M^2 \cos(2\Omega_R t) - 4t\delta^2\Omega_R \sin(\Omega_R t) \right), \\ g_{tt} &= \frac{M^2}{8\Omega_R^4} \left(2(4k^2 + M^2)^2 - 8k(4k^2 + M^2)\Omega + (16k^2 + M^2)\Omega^2 - 8k\Omega^3 + 2\Omega^4 \right. \\ &\quad \left. + 4\delta\Omega(4k^2 + M^2 - 2k\Omega) \cos(\Omega_R t) - M^2\Omega^2 \cos(2\Omega_R t) \right), \\ g_{kt} &= \frac{M^2}{4\Omega_R^6} \left(-2t\delta(4k^2 + M^2 - 2k\Omega)\Omega_R^2 - 2t\Omega\delta^2\Omega_R^2 \cos(\Omega_R t) \right. \\ &\quad \left. - 2\Omega_R \left(2k(4k^2 + M^2) - 2(6k^2 + M^2)\Omega + 6k\Omega^2 - \Omega^3 + M^2\Omega \cos(\Omega_R t) \right) \sin(\Omega_R t) \right), \\ \Omega_{kt} &= \frac{M^2}{\Omega_R^4} \left(-(4k^2 + M^2 - \Omega^2)(-1 + \cos(\Omega_R t)) - t\Omega\delta\Omega_R \sin(\Omega_R t) \right). \end{aligned} \quad (29)$$

From these expressions, we see that momentum component of the metric g_{kk} oscillates and also grows quadratically with time, reminiscing the first row of Fig. 2; The temporal component g_{tt} follows the oscillation of the drive, which coincides with the behavior in the second row of Fig. 2; The mixed component g_{kt} oscillates and increases linearly with time, in agreement with the third row of Fig. 2; Finally, the mixed component Berry curvature Ω_{kt} oscillates and also has some component linear in time, which seems to capture some features in the fourth and fifth row of Fig. 2. Our investigation thus reveals a rather similar time dependence of quantum geometry in driven two-state systems, regardless of how it is driven.

The Fisher information matrix can be calculated in the same manner, yielding

$$\begin{aligned}
I_{kk} &= \frac{4M^2\delta^2 (4 + t^2\Omega_R^2 + (-4 + t^2\Omega_R^2) \cos(\Omega_R t) - 4t\Omega_R \sin(\Omega_R t))}{\Omega_R^4 (M^2 + 2\delta^2 + M^2 \cos(\Omega_R t))}, \\
I_{tt} &= \frac{2M^2\Omega_R^2 \cos^2(\Omega_R t/2)}{M^2 + 2\delta^2 + M^2 \cos(\Omega_R t)}, \\
I_{tk} &= -\frac{2M^2\delta (\Omega_R t + \Omega_R t \cos(\Omega_R t) - 2 \sin(\Omega_R t))}{\Omega_R (M^2 + 2\delta^2 + M^2 \cos(\Omega_R t))},
\end{aligned} \tag{30}$$

leading to a vanishing volume form $\sqrt{\det I_{\mu\nu}} = \sqrt{I_{tt}I_{kk} - I_{tk}^2} = 0$. Our results indicate that the momentum component I_{kk} oscillates and increases quadratically with time, which seems to coincide with the second row of Fig. 4 during the pulse period; The temporal component I_{tt} simply follows the oscillation, which also reflects the behavior during the pulse in the third row of Fig. 4; The mixed component I_{kt} oscillates and linearly increases with time, reminiscing the peculiar shape in the fourth row of Fig. 4 that does not completely follow the pulse shape. Thus the information geometric properties of driven quantum systems may also display somewhat universal features irrespective of the details of the drive.

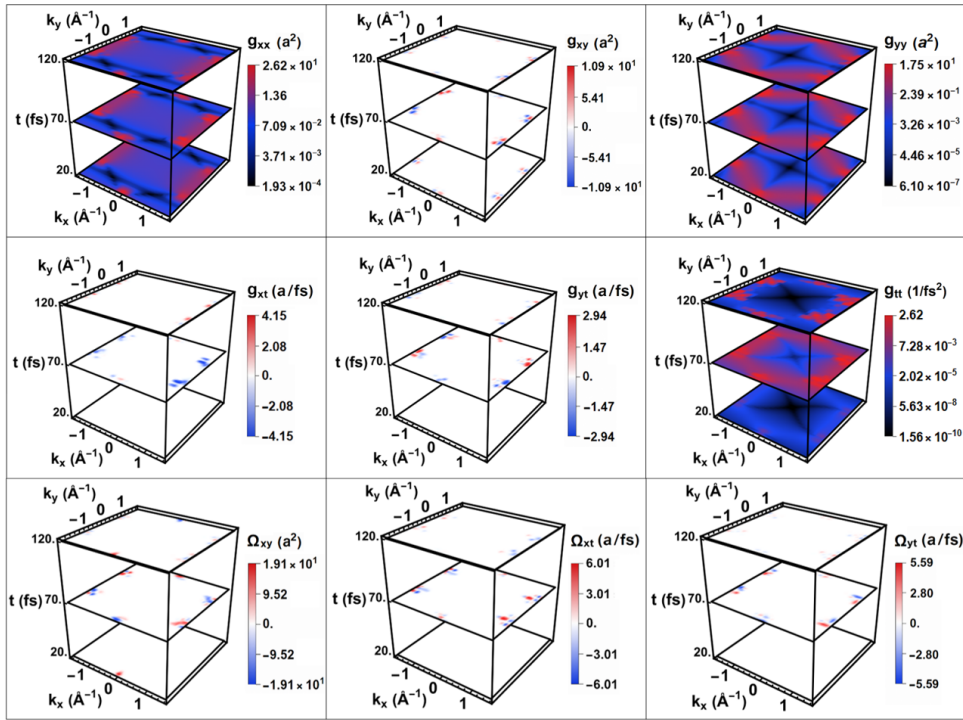


Figure 5: The momentum-time pattern of the components of the dynamic quantum geometric tensor in a wider momentum space that covers the first Brillouin zone, evaluated at three time slices representing before the pulse maximum $t = 20$ fs, peak of the pulse $t = 70$ fs, and after the pulse $t = 120$ fs. The components are labeled at each panel.

B Dynamic quantum geometry in the whole Brillouin zone

In Figure 5, we present all the components of the quantum metric and Berry curvature in the whole Brillouin zone, at three time slices corresponding to the beginning of the pulse $t = 20$ fs, peak of the pulse 70 fs, and right after the pulse 120 fs. While there is some contribution throughout the whole Brillouin zone, the figure indicates that the maxima of the quantum metric and Berry curvature are always located around the K and K' valleys.

References

- [1] J. P. Provost and G. Vallee. Riemannian structure on manifolds of quantum states. *Comm. Math. Phys.*, 76(3):289–301, 1980.
- [2] M. V. Berry. Quantal phase factors accompanying adiabatic changes. *Proc. R. Soc. A*, 392(1802):45–57, 1984.
- [3] Di Xiao, Ming-Che Chang, and Qian Niu. Berry phase effects on electronic properties. *Rev. Mod. Phys.*, 82:1959–2007, July 2010.
- [4] Tomoki Ozawa and Nathan Goldman. Extracting the quantum metric tensor through periodic driving. *Phys. Rev. B*, 97:201117, May 2018.
- [5] Junyeong Ahn, Guang-Yu Guo, Naoto Nagaosa, and Ashvin Vishwanath. Riemannian geometry of resonant optical responses. *Nat. Phys.*, 18(3):290–295, Mar 2022.
- [6] Ilia Komissarov, Tobias Holder, and Raquel Queiroz. The quantum geometric origin of capacitance in insulators. *Nature Communications*, 15(1):4621, May 2024.
- [7] Wei Chen. Dielectric and optical markers originating from quantum geometry. *Phys. Rev. B*, 111:085202, Feb 2025.
- [8] C. De Grandi, V. Gritsev, and A. Polkovnikov. Quench dynamics near a quantum critical point. *Phys. Rev. B*, 81:012303, Jan 2010.
- [9] C. De Grandi, V. Gritsev, and A. Polkovnikov. Quench dynamics near a quantum critical point: Application to the sine-gordon model. *Phys. Rev. B*, 81:224301, Jun 2010.
- [10] Shengshi Pang and Andrew N. Jordan. Optimal adaptive control for quantum metrology with time-dependent hamiltonians. *Nature Communications*, 8(1):14695, Mar 2017.
- [11] R. Jafari and Alireza Akbari. Dynamics of quantum coherence and quantum fisher information after a sudden quench. *Phys. Rev. A*, 101:062105, Jun 2020.
- [12] Shuohang Wu, Zhengxin Guo, Zijian Xiong, Yuan Yao, and Zi Cai. Universal critical dynamics of quantum geometry, 2024. arXiv:2401.17885.
- [13] Bogar Díaz, Diego Gonzalez, Marcos J. Hernández, and J. David Vergara. Time-dependent quantum geometric tensor and some applications, 2025. arXiv:2502.01788.
- [14] Jahan M. Dawlaty, Shriram Shivaraman, Mvs Chandrashekhara, Farhan Rana, and Michael G. Spencer. Measurement of ultrafast carrier dynamics in epitaxial graphene. *Appl. Phys. Lett.*, 92(4):042116, 01 2008.
- [15] Haining Wang, Jared H. Strait, Paul A. George, Shriram Shivaraman, Virgil B. Shields, Mvs Chandrashekhara, Jeonghyun Hwang, Farhan Rana, Michael G. Spencer, Carlos S. Ruiz-Vargas, and Jiwoong Park. Ultrafast relaxation dynamics of hot optical phonons in graphene. *Appl. Phys. Lett.*, 96(8):081917, 02 2010.
- [16] M. Breusing, S. Kuehn, T. Winzer, E. Malić, F. Milde, N. Severin, J. P. Rabe, C. Ropers, A. Knorr, and T. Elsaesser. Ultrafast nonequilibrium carrier dynamics in a single graphene layer. *Phys. Rev. B*, 83:153410, Apr 2011.
- [17] Jared H. Strait, Haining Wang, Shriram Shivaraman, Virgil Shields, Michael Spencer, and Farhan Rana. Very slow cooling dynamics of photoexcited carriers in graphene observed by optical-pump terahertz-probe spectroscopy. *Nano Lett.*, 11(11):4902–4906, Nov 2011.

- [18] S. Winnerl, M. Orlita, P. Plochocka, P. Kossacki, M. Potemski, T. Winzer, E. Malic, A. Knorr, M. Sprinkle, C. Berger, W. A. de Heer, H. Schneider, and M. Helm. Carrier relaxation in epitaxial graphene photoexcited near the dirac point. *Phys. Rev. Lett.*, 107:237401, Nov 2011.
- [19] K. J. Tielrooij, J. C. W. Song, S. A. Jensen, A. Centeno, A. Pesquera, A. Zurutuza Elorza, M. Bonn, L. S. Levitov, and F. H. L. Koppens. Photoexcitation cascade and multiple hot-carrier generation in graphene. *Nat. Phys.*, 9(4):248–252, Apr 2013.
- [20] Jens Christian Johannsen, Søren Ulstrup, Federico Cilento, Alberto Crepaldi, Michele Zacchigna, Cephise Cacho, I. C. Edmond Turcu, Emma Springate, Felix Fromm, Christian Roidel, Thomas Seyller, Fulvio Parmigiani, Marco Grioni, and Philip Hofmann. Direct view of hot carrier dynamics in graphene. *Phys. Rev. Lett.*, 111:027403, Jul 2013.
- [21] Isabella Gierz, Jesse C. Petersen, Matteo Mitrano, Cephise Cacho, I. C. Edmond Turcu, Emma Springate, Alexander Stöhr, Axel Köhler, Ulrich Starke, and Andrea Cavalleri. Snapshots of non-equilibrium dirac carrier distributions in graphene. *Nat. Mater.*, 12(12):1119–1124, Dec 2013.
- [22] D. Brida, A. Tomadin, C. Manzoni, Y. J. Kim, A. Lombardo, S. Milana, R. R. Nair, K. S. Novoselov, A. C. Ferrari, G. Cerullo, and M. Polini. Ultrafast collinear scattering and carrier multiplication in graphene. *Nat. Commun.*, 4(1):1987, Jun 2013.
- [23] S Winnerl, F Göttfert, M Mittendorff, H Schneider, M Helm, T Winzer, E Malic, A Knorr, M Orlita, M Potemski, M Sprinkle, C Berger, and W A de Heer. Time-resolved spectroscopy on epitaxial graphene in the infrared spectral range: relaxation dynamics and saturation behavior. *J. Phys. Condens. Matter*, 25(5):054202, jan 2013.
- [24] T. Plötzing, T. Winzer, E. Malic, D. Neumaier, A. Knorr, and H. Kurz. Experimental verification of carrier multiplication in graphene. *Nano Lett.*, 14(9):5371–5375, Sep 2014.
- [25] Martin Wagner, Zhe Fei, Alexander S. McLeod, Aleksandr S. Rodin, Wenzhong Bao, Eric G. Iwinski, Zeng Zhao, Michael Goldflam, Mengkun Liu, Gerardo Dominguez, Mark Thiemens, Michael M. Fogler, Antonio H. Castro Neto, Chun Ning Lau, Sergiu Amarie, Fritz Keilmann, and D. N. Basov. Ultrafast and nanoscale plasmonic phenomena in exfoliated graphene revealed by infrared pump–probe nanoscopy. *Nano Lett.*, 14(2):894–900, Feb 2014.
- [26] I. Gierz, F. Calegari, S. Aeschlimann, M. Chávez Cervantes, C. Cacho, R. T. Chapman, E. Springate, S. Link, U. Starke, C. R. Ast, and A. Cavalleri. Tracking primary thermalization events in graphene with photoemission at extreme time scales. *Phys. Rev. Lett.*, 115:086803, Aug 2015.
- [27] M. A. Sentef, M. Claassen, A. F. Kemper, B. Moritz, T. Oka, J. K. Freericks, and T. P. Devereaux. Theory of floquet band formation and local pseudospin textures in pump-probe photoemission of graphene. *Nature Communications*, 6(1):7047, May 2015.
- [28] Michael Schüler and Michael A. Sentef. Theory of subcycle time-resolved photoemission: Application to terahertz photodressing in graphene. *J. Electron Spectrosc. Relat. Phenom.*, 253:147121, 2021.
- [29] Marco Merboldt, Michael Schüler, David Schmitt, Jan Philipp Bange, Wiebke Bennecke, Karun Gadge, Klaus Pierz, Hans Werner Schumacher, Davood Momeni, Daniel Steil, Salvatore R. Manmana, Michael A. Sentef, Marcel Reutzler, and Stefan Mathias. Observation of floquet states in graphene. *Nat. Phys.*, 21(7):1093–1099, Jul 2025.

-
- [30] Milena Grifoni and Peter Hänggi. Driven quantum tunneling. *Physics Reports*, 304(5):229–354, 1998.
- [31] S. Amari. *Information Geometry and Its Applications*. Springer, February 2016.
- [32] R. A. Fisher. Theory of statistical estimation. *Math. Proc. Camb. Philos. Soc.*, 22(5):700–725, 1925.
- [33] Paolo Facchi, Ravi Kulkarni, V.I. Man’ko, Giuseppe Marmo, E.C.G. Sudarshan, and Franco Ventriglia. Classical and quantum fisher information in the geometrical formulation of quantum mechanics. *Physics Letters A*, 374(48):4801–4803, 2010.
- [34] A. H. Castro Neto, F. Guinea, N. M. R. Peres, K. S. Novoselov, and A. K. Geim. The electronic properties of graphene. *Rev. Mod. Phys.*, 81:109–162, Jan 2009.
- [35] Denis Kochan, Susanne Irmer, and Jaroslav Fabian. Model spin-orbit coupling hamiltonians for graphene systems. *Phys. Rev. B*, 95:165415, Apr 2017.
- [36] Gero von Gersdorff and Wei Chen. Measurement of topological order based on metric-curvature correspondence. *Phys. Rev. B*, 104:195133, Nov 2021.
- [37] Tran Trung Luu and Hans Jakob Wörner. Measurement of the berry curvature of solids using high-harmonic spectroscopy. *Nat. Commun.*, 9(1):916, Mar 2018.
- [38] Wei Chen and Gero von Gersdorff. Measurement of interaction-dressed berry curvature and quantum metric in solids by optical absorption. *SciPost Phys. Core*, 5:040, 2022.
- [39] Mingu Kang, Sunje Kim, Yuting Qian, Paul M. Neves, Linda Ye, Junseo Jung, Denny Puntel, Federico Mazzola, Shiang Fang, Chris Jozwiak, Aaron Bostwick, Eli Rotenberg, Jun Fuji, Ivana Vobornik, Jae-Hoon Park, Joseph G. Checkelsky, Bohm-Jung Yang, and Riccardo Comin. Measurements of the quantum geometric tensor in solids. *Nat. Phys.*, 21(1):110–117, Jan 2025.